UNIVERSITI TEKNOLOGI MARA
Cawangan Kedah
Kampus Sungai Petani

2021 iCMS
INTERNATIONAL CONFERENCE ON COMPUTING, MATHEMATICS AND STATISTICS

e-PROCEEDINGS

of The 5th International Conference on Computing, Mathematics and Statistics (iCMS2021)

4-5 August 2021

Driving Research Towards Excellence

e-Proceedings of the 5th International Conference on Computing, Mathematics and Statistics (iCMS 2021)

Driving Research Towards Excellence

Editor-in-Chief: Norin Rahayu Shamsuddin

Editorial team:
Dr. Afida Ahamad
Dr. Norliana Mohd Najib
Dr. Nor Athirah Mohd Zin
Dr. Siti Nur Alwani Salleh
Kartini Kasim
Dr. Ida Normaya Mohd Nasir
Kamarul Ariffin Mansor

e-ISBN: 978-967-2948-12-4
DOI

Library of Congress Control Number:

Publication by
Department of Mathematical Sciences
Faculty of Computer & Mathematical Sciences
UiTM Kedah

TABLE OF CONTENT

PART 1: MATHEMATICS

PART 2: STATISTICS

PART 3: COMPUTER SCIENCE & INFORMATION TECHNOLOGY

PART 4: OTHERS

A 1D Eye Tissue Model to Mimic Retinal Blood Perfusion during Retinal Imaging Photoplethysmography (iPPG) Assessment: A Diffusion Approximation – Finite Element Method (FEM) Approach

Harnani Hassan[1], Sukreen Hana Herman[1], Zulfakri Mohamad[1,2], Sijung Hu[3] and Vincent M. Dwyer[3]

[1] Integrated Sensor Research Group (DERIA), School of Electrical Engineering, College of Engineering, Universiti Teknologi MARA, 40450 Shah Alam, Selangor, MALAYSIA, [2] Research Center for Neutrino Science (RCNS), Tohoku University, Sendai, 980-8578, JAPAN, [3] Photonics Engineering and Health Technology Group, Loughborough University, LE11 3TU, UK

([1] harnani@uitm.edu.my , [2] hana1617@uitm,edu.my , [3]zulfakri@uitm.edu.my ,[4] S.Hu@lboro.ac.uk, [5] V.M.Dwyer@lboro.ac.uk)

This paper presents a one-dimension (1D) eye tissue model to mimic retinal blood perfusion during retinal imaging photoplethysmography (iPPG) assessment in previous work. An uneven light source illumination and noise during the assessment can affect the extraction of backscattering light, hence alter the actual blood perfusion measurement. In this work, a simplified eye model that consists of four layers: retina, retina epithelium (RPE), choroid, and sclera was employed to perform numerical analysis using diffusion approximation – Finite Element Method (FEM) approach. The analysis has utilized optical properties of healthy eye tissue and the simulation was performed in the MATLAB 2019a environment. The outcomes of alternate current (AC) component and fluence rate show that the proposed approach can be utilized to mimic retinal blood perfusion in different tissue depths and predict the amplitude of the generated pulsatile waveform before starting an assessment. The simulation consumed less computation time to analyze and the generated pulsatile was uncontaminated with noise.

***Keywords*:** numerical analysis, eye tissue model, retinal blood perfusion, retinal imaging photoplethysmography (iPPG), diffusion approximation, Finite Element Method (FEM).

1. Introduction

Over the years, the diagnostic and therapeutic application of such spectroscopy, endoscopy, and tomography utilizes photon distribution information to identify abnormalities in tissue, blood perfusion in a blood vessel, oxygen level, tissue degeneration, and tumor (Fass, 2008)(Beyer et al., 2020). The characterization and detection of tissue abnormalities can be achieved by an in-depth understanding of light propagation in turbid media. The light propagation through turbid media obeys Maxwell's equation that describes electromagnetic fields together with reasonable and simplifying assumptions (Steven L Jacques, 2013)(Steven L Jacques & Pogue, 2008). The light transport theory adopts statistical mechanics to describe light behavior as photons travel through a scattering medium. The theory measures the averages scattering particles with a probability density function, rather than a deterministic function(S L Jacques, 1998). The theory is called Radiative Transfer Theory (RTE) when it is applied to low energy photons with several simplification assumptions, (i) wave effects such as diffraction and interference can be neglected, and (ii) all photons have the same energy where the scattering is elastic. Therefore, a tissue model is developed using a numerical method to quantify the distribution of light intensity in tissue by solving Radiative Transfer Theory (RTE) (Tarvainen et al., 2006). The numerical method probably offers the best approach to solve RTE turbid media with complex boundaries and various interior properties (x,y,z). The numerical methods can include the analytical or semi-analytical methods, Finite Element Methods (FEM), Finite Different Methods (FDM), and Boundary Element Methods (BEM), and Monte Carlo (MC) methods (Handapangoda, 2017) . The Monte Carlo (MC method is one of the most common numerical methods used to quantify the light distribution in the tissue, other than the Finite Element Method (FEM) and Finite Different Method (FDM) (Handapangoda, 2017)(Kim & Keller, 2003). Even though these methods work very well to quantify light

distribution in tissue with complex boundaries and various interior properties (x,y,z), the method suffers stochastic noise that inherits due to repetitive iteration process (Haskell et al., 1994). Besides, the method takes a longer computation time to track the numbers of a photon in the tissue once it is launched.

In this work, a 1D diffusion approximation – Finite Element Method (FEM) was considered to provide quick analysis to predict blood perfusion in eye tissue without stochastic noise removal. The computation time was quick which approximately less than 2 minutes compared to other numerical analysis methods. This method was used to produce a time-varying AC signal that mimics the blood perfusion in different tissue layers: (i) retina and (ii) choroid during retinal imaging photoplethysmography (iPPG) assessment. The fundamental issue for tissue modeling is the understanding of the nature of the light distribution in the retina caused by: (i) scattering and absorption within layers due to the layer's optical properties and (ii) at layer boundaries due to differences in the reflective index (Haskell et al., 1994)(Steven L Jacques & Pogue, 2008)**.** The development of tissue modeling requires knowledge of the ocular structure and its components in addition to those optical properties. Also, other factors such as race, gender, age, and health condition will influence the optical properties value as reported in the previous studies (Atchison et al., 2008)**.** Retinal photoplethysmography (iPPG) is an optical technique that used 2-by-2 sequences of colored fundus images to capture the blood volume during cardiac activity (Hassan et al., 2018)(D.J., 2012)**.** The images are processed using an image processing technique to extract the iPPG signal from the Green (G) channel. The outcomes of this work can be used to implement quick analysis and predict blood perfusion within a shorter computation time.

2. Methodology

In this work, a complex eye tissue layer was simplified into 1D tissue layer consist of four main layers; (i) Retinal epithelium (RPE), retina, choroid, and sclera (Eliasdottir, 2018). The eye blood network is unique where it has two blood networks: (i) retina and (ii) choroid (Eliasdottir, 2018), to carry nutrients, enzymes, oxygen to the eye tissue and also to maintain the intraocular pressure (IOP) in the eye (Tornow et al., 2021)**.** Therefore, the light interaction in the tissue was concerned about the volume of blood flow in the retina and choroid layer during the cardiac activity.

2.1 Eye Tissue Model

The ocular tissue layers are complex by nature. The ocular tissue can be divided into (i) ocular media and (ii) ocular fundus (Hani et al., 2009)**.** The ocular media consist of a pupil, aqueous humour, lens, cornea, and vitreous humour, while the ocular fundus is consisting of (i) retina, (ii) retinal pigment epithelium (RPE), (iii) choroid, and (iv) sclera (Hani et al., 2009)**.** In this study, the tissue modelling is underlaying the understanding of light interaction in the retina caused by (i) absorption, and (ii) scattering that occurred within the layers due to the layer's optical properties; and (ii) at the layer boundaries due to differences of the reflective index (Haskell et al., 1994)**.** The ocular fundus was considered to implement numerical analysis of light interaction in the tissue using the diffusion approximation-FEM approach and solve Radiative Transfer Theory (RTE). The light interaction in the eye tissue model was illustrated in **Figure 1**.

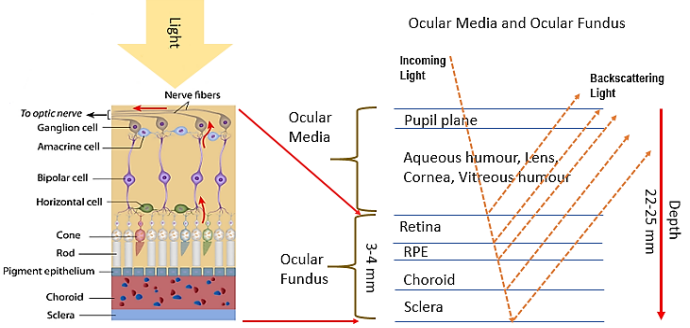

Figure 1: Eye tissue model

In the figure, four layers of eye tissue (i) retina, (ii) RPE, (iii) choroid, and (iv) sclera are considered to quantify light interaction in the tissue due to absorption and scattering events. The light interaction depends on the optical properties (i) reduced scattering coefficient, μ_s', (ii) absorption coefficient, μ_a, (iii) phase function, g, (iv) thickness, d, and the mismatch of the reflective index, η between layers that changes as the light penetrated deeper into the tissue layer (Haskell et al., 1994)(Steven L Jacques, 2013).

The light interaction due to absorption and scattering events of photon propagation because more diffuse as the light penetrates deeper into the tissue. The emitted photons that escaped the tissue surface carried the information of blood flowing in the blood vessel that is interpreted in an alternate current (AC) signal (Morgan et al., 2015). The amplitude of produced AC signal represents the blood perfusion in the retinal blood vessel. The blood perfusion of the eye is produced from two blood networks (i) retina and (ii) choroid (Hani et al., 2009)(Morgan et al., 2014). In this study, a blood vessel was embedded in (i) the retina and (ii) the choroid layer as illustrated in **Figure 2**. The 1D tissue models were developed with a specific optical parameter setting as tabulated in **Table 1**.

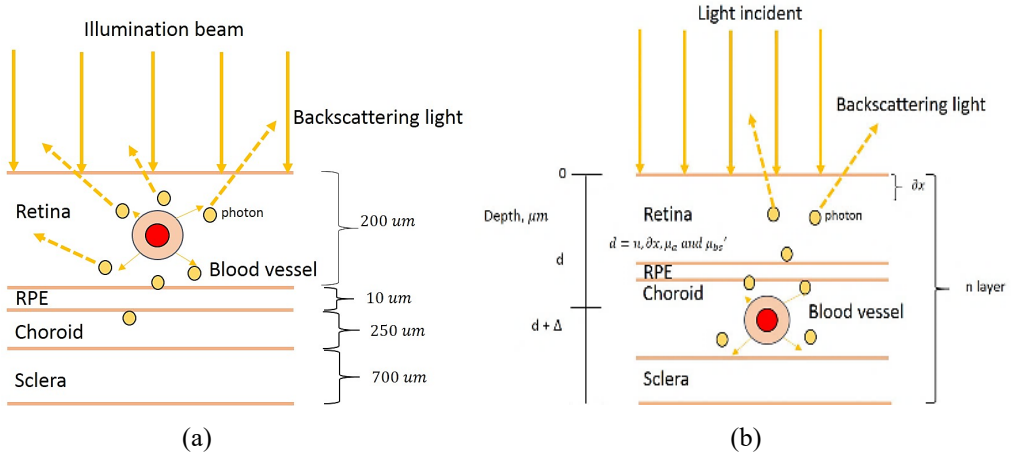

Figure 2: Single event of light absorption and backscattering with *d*; depth, *dx*; light distribution at *n* layer; μ_a; absorption coefficient and $\mu_{bs}{}'$; backscattering coefficient, (a) 1D eye tissue model with a blood vessel embeds in retina layer, (b) 1D eye tissue model blood vessel embeds in the choroid layer.

2.2 Optical Properties Setting for Eye Tissue

Table 1 illustrates the optical properties of (i) reduced scattering coefficient, μ_s', (ii) absorption coefficient, μ_a, (iii) phase function of Henyey-Greenstein, g, and thickness, d for healthy eye tissue (Liu et al., 2013). The Henyey-Greenstein phase function, g represents the scattering direction that is normalized for forward-scattering with, $g = +1$ (Henyey & Greenstein, 1941)(Steven L Jacques & Pogue, 2008). The optical properties of eye tissue were set up for healthy eye tissue where the blood vessel position was embedded in (i) retina and (ii) choroid layer (D.J., 2012)(Hani et al., 2009).

Table 1: Optical properties of a 1D diffusion approximation-FEM approach model

Blood vessel position (embedded)	Retinal Tissue Layers	Thickness of Healthy Tissue (μm)	Healthy Tissue	
			(μ_a) (mm^{-1})	($\mu_{s'}$) (mm^{-1})
Retina (Case I)	Retina	70	0.147	3.10
	Blood	60	23.8	70
	RPE	10	63	115.8
	Choroid	250	8.383	61.53

	Sclera	700	0.4	89.8
Choroid (Case II)	Retina	200	0.147	3.10
	RPE	10	63	115.8
	Choroid	95	8.383	61.53
	Blood	60	238	70
	Sclera	700	0.4	89.8

2.3 Diffusion Approximation – FEM Approach

The 1D eye tissue was modeled in the *z*-direction where a diffusion approximation-FEM approach was applied to quantify blood flowing in the blood vessel which is interpreted as the amplitude of AC signal. The algorithm of the 1D diffusion approximation – FEM model starts with the (i) understanding of light interaction in the tissue, (ii) the assumption and definition of RTE for blood vessel derivation, (iii) solving the RTE with diffusion approximation-FEM approach, (iv) solve the boundary condition of P_1 approximation and (v) transport approximation for a time-varying scattering of AC signal component.

2.31 Light interaction and matter in the tissue

The light interaction in the tissue is quantified from the scattering and absorption events, reflective index, η and phase function, g. The refractive index, η is the ratio of light velocity in vacuum to the velocity of light in a specified medium. The refractive index, η in (2.31) is defined by adding a complex refractive index, $j\eta''$ to the real η' also involves the energy dissipation (absorption) in the biological media (Steven L Jacques, 2013).

$$\eta = \eta' + j\eta'' \tag{2.31}$$

η' is the real part of the refractive index that describes energy storage and affects the speed of light in the medium. The imaginary refractive index, $j\eta''$defines the energy dissipation and absorption coefficient, $\mu_a = 4\pi\eta''/\lambda$ at the specified wavelength, λ. The energy dissipation in a certain depth, x of the tissue may be included in the electric field of the light plane wave. This electric field of a light plane wave is represented by the phasor $E = E_0\exp(j\underline{K}.\underline{r})$, or $E = E_0\exp(jK.x)$ in 1D tissue model with spatial frequency, K or wave number (Dwyer & Matthew, 1985) The electric field becomes $\exp(\frac{2\pi jx}{\lambda})$ in terms of the wavelength, λ and in a medium of refractive index, η it becomes $\exp\left(\frac{2\pi j\eta x}{\lambda}\right)$ where the wavelength changes from λ to $\frac{\lambda}{\eta}$ .Substituting (2.31) into the equation, the electric field, $E = E_0\exp(\frac{2\pi j\eta' x}{\lambda})\exp(-\frac{2\pi\eta'' x}{\lambda})$ and the intensity, $I = |E|^2$ behaves as $\exp\left(-\frac{4\pi\eta'' x}{\lambda}\right) = \exp(-\mu_a x)$, as expected. Assuming that the value of η' is made of two contributions of dry tissue and water content, a first approximation presented in (2.32) is defined as follows,

$$\begin{aligned}\eta' &= \eta'_{dry}(1-W) - \eta'_{water}W \\ &= \eta'_{dry} - (\eta'_{dry} - \eta'_{water})W\end{aligned} \tag{2.32}$$

where W is a fraction of water-like tissue, η'_{dry} is the refractive index of the tissue's dry mass and η'_{water} is the refractive index of water-like material in the tissue (Steven L Jacques & Pogue, 2008).

The scattering coefficient, $\mu_s = -\ln(T_c)/L$ represents the probability of photon scattering in tissue, per unit path length and usually obtained from a collimated transmission measurement, T_c

through the tissue of thickness, L. However, the measurement must be implemented on a thin tissue sample ($\leq 100\ \mu m$) to obtain a scattering mean free path $mfp = 1/\mu_s$ that larger than L to avoid the possibility of too much multiple scattering (Rodmell et al., 2014)(S L Jacques, 1998). In addition, there is an issue regarding the experimental preparation of thin tissue because the tissue is easily exposed to dryness, detector angle and the type of tissue to be tested either a homogenous or heterogeneous tissue is likely to affect the measurement results (Steven L Jacques & Pogue, 2008). The attenuation of light in deep biological tissue depends on the effective attenuation coefficient μ_{eff}, as expressed in (2.33):

$$\mu_{eff} = \sqrt{3\mu_a\,(\mu_a + \mu_s')} \xrightarrow[\mu_a \ll \mu_s']{} \sqrt{3\mu_a\,\mu_s'} \tag{2.33}$$

where μ_s' denoted as transport scattering coefficient or reduced scattering coefficient; $\mu_s' = \mu_s(1-g)$ with phase function anisotropy, $g$of biological tissue. The effective attenuation coefficient, μ_{eff} is the dominant factor for determining light attenuation at depth, $x \gg 1/\mu_s'$. The anisotropy, g is used to describe the condition of scattering properties that depend on the direction of the incoming beam and vary systematically (Steven L Jacques & Pogue, 2008). The anisotropy, g is equal to the mean of the cosine of the scattering angle, $\langle \cos(\theta) \rangle$; if $g = 1$ then $\theta = 0$ and the scattering is forward, while if $g = 0$ then equal amounts of light are scattered forward $\langle \cos\theta \rangle > 0$ and backward $\langle \cos\theta \rangle < 0$. The measurement of anisotropy, g is experimentally complex, as several issues need to be concerned especially involving thin tissue samples and light scattering angular that need to be defined during the measurement. Therefore, one of the approaches to measuring anisotropy, g in a biological tissue using the reduced scattering coefficient, μ_s' and scattering coefficient, μ_a from the collimated transmission, μ_s that deduced value of anisotropy g in (2.34) (Simon et al., 2013),

$$g = 1 - \frac{\mu_s'}{\mu_s} \tag{2.34}$$

The reduced scattering, μ_s' interpretation is applied (i) if there are many scattering events before an absorption event, i.e., $\mu_a \ll \mu_s'$, then the limit on the right of (2.33) to describe the diffusion of photons in a random walk of step size of $1/\mu_s'$ [cm] and (ii) each step involves isotropic scattering ($g = 0$) or a biased random walk ($g \neq 0$) (Simon et al., 2013). The interpretation is equivalent to a description of photon movement using many small steps $1/\mu_s$ that each involves only a partial deflection angle θ, i.e., and replaces many small-angle scattering events with a single isotropic one. In this situation, the scattering-dominated light transport is called the diffusion regime and μ_s' which is useful in the diffusion regime to demonstrate light propagates through biological tissues in the visible and near-infrared ranges.

The normal range of anisotropy, g is between 0.8 to 0.98 where higher values allow high concentration of light to propagate in the forward direction and avoiding multiple scattering (Simon et al., 2013). However, high anisotropy, g values reduce the amount of backscattered light on the targeted tissue and this affects the collected reflected light. Therefore, the reflectance measurement depends on two parameters (1) attenuation (μ_{eff} cm^{-1}) over depth, x and (ii) absolute value of reflected signal within the focus. The scattering in biological tissue is commonly described using the Henyey–Greenstein phase function with anisotropy, g. The phase function describes the probability $p(\theta)$ of a scattering event with a scattering angle, θ (Simon et al., 2013). The Henyey–Greenstein phase function is expressed in (2.35):

$$p(\theta) = \frac{1}{4}\frac{1 - g^2}{(1 + g^2 - 2g\cos\theta)^{3/2}}$$

The function is rewritten as in (2.35) with cos (θ),

$$p(\cos\theta) = \frac{1}{2}\frac{1 - g^2}{(1 + g^2 - 2g\cos\theta)^{3/2}} \tag{2.35}$$

Continuing with (2.35) the probability $p(\theta)$ of scattering event is expressed as follows,

$$\int_{-1}^{1} p(cos\,\theta)d(cos\,\theta) = 1$$

$$\int_{-1}^{1} p(\cos\theta)\cos\theta\, d(\cos\theta) = g \tag{2.36}$$

The Henyey–Greenstein phase function imitates the angular dependence of light scattering by particles, for various values of the anisotropy g. The forward direction, (i) photon trajectory can be specified as 0° degrees, and (ii) 180° degrees for backward scattering direction where the curve of the phase function, $g = 0$ remains constant and equal to $1/2$.

The absorption coefficient, μ_a describes the probability of propagating light being absorbed by an absorbing medium, or tissue, per unit path length in the function of wavelength, λ. The absorption coefficient, $\mu_a(cm^{-1})$ may be expressed as in (2.37),

$$\mu_a = -\frac{1}{T}\frac{dT}{dl} = -\frac{d\log(T)}{dl} \tag{2.37}$$

where T (dimensionless) defined as the fraction of light still propagating in the tissue after travelled a path length of l (cm) (Steven L Jacques, 2013)**.** The fraction change of light propagation is obtained by integration as expressed in (2.38),

$$T = e^{-\mu_a l} = 10^{-\varepsilon C l} = e^{-4\pi\eta'' l/\lambda} \tag{2.38}$$

where C represents the concentration value of chromophores (mol L^{-1}) and the ε is the molar extinction coefficient, (cm^{-1} M^{-1}). The chromophores (absorbers) such as water, blood, melanin, fat or lipid, and collagen (Steven L Jacques, 2013)(S L Jacques, 1998) absorb the light at certain wavelengths and are commonly used to interpret the photon absorption in tissue. Therefore, for N of absorbing chromophores, the absorption coefficient, μ_a in tissue is expressed as (2.39),

$$\mu_a = \ln(10)\sum_{k=1}^{N} \varepsilon_k\,(\lambda_x)\,.\,C_k \tag{2.39}$$

where μ_a represents the total absorption coefficient, λ_x is the wavelength, C_k and ε_k are the molar extinction coefficient and concentration of chromophore k.

2.4 RTE assumption and definition for the ocular tissue model

The radiative transport equation (RTE) for the ocular tissue model assumption and definition are described as follows,

(i) The radiance $I(\vec{r}, \hat{\Omega}, t)$ represents the energy flow per unit normal area, per unit solid angle, and per unit time (Haskell et al., 1994)(Steven L Jacques & Pogue, 2008)**.** In **Figure 3**, the energy flow into an area $\overrightarrow{\delta A} = \delta A\vec{n}$, in time dt, from an incident beam, at an angle $\hat{\Omega}$, is $\overrightarrow{\delta A}.\hat{\Omega}I(\vec{r}, \hat{\Omega}, t)dt$. The total energy crossing a surface, $\overrightarrow{\delta A} = \delta A(0,0,1)$ is the integral overall $\hat{\Omega}$ as in (2.41),

$$\overrightarrow{\delta A}.\int_{\hat{\Omega}} \hat{\Omega}I(\vec{r}, \hat{\Omega}, t)d\hat{\Omega} = \delta A\int_{0}^{\pi}\cos(\theta)\sin(\theta)d\theta\int_{0}^{2\pi} I(\vec{r}, \hat{\Omega}, t)d\psi \tag{2.41}$$

(ii) The fluence rate or flux at $\vec{r}$, is the total radiance integrated overall angle. I.e., $\Phi(\vec{r}, t) = \int_{\hat{\Omega}} I(\vec{r}, \hat{\Omega}, t)d\hat{\Omega}$.

(iii) The current density at $\vec{r}$, i.e. $J(\vec{r},t) = \int_{\widehat{\Omega}} \widehat{\Omega} I(\vec{r},\widehat{\Omega},t) d\widehat{\Omega}$, is the net energy flow per unit area, per unit time. This contributes to (2.41) from the angles $0 \leq \theta < \pi/2$ with $I_{+}(\vec{r},\widehat{\Omega},t)$) corresponds to $\cos(\theta) > 0$ and positive current density from $\pi/2 < \theta \leq \pi$ ($I_{-}(\vec{r},\widehat{\Omega},t)$) that corresponds to the current out (Haskell et al., 1994)(Chandrasekhar., 1950).

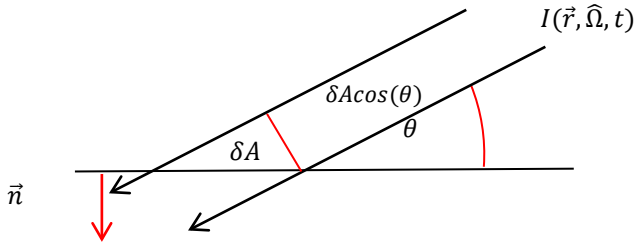

Figure 3: Beam at elevation angle θ, and azimuth ψ

2.5 RTE derivation for the blood vessel

The RTE derivation for the blood vessel can be interpreted as an energy balance in a cylinder geometry (Hassan et al., 2015) as illustrated in **Figure 4**. The energy balance in **Figure 4** is expressed as the volume of blood = $ds \times$ unit cross-sectional area where,

(i) The convective change in $I(\vec{r},\widehat{\Omega},t)$ in travelling an infinitesimal distance ds with velocity $c\widehat{\Omega}$, in time $dt = ds/c$, is denoted by (2.42);

$$dI(\vec{r},\widehat{\Omega},t) = I(\vec{r} + c\widehat{\Omega}dt, \widehat{\Omega}, t + dt) - I(\vec{r},\widehat{\Omega},t) = \left(\frac{\partial I(\vec{r},\widehat{\Omega},t)}{\partial t} + c\widehat{\Omega}.\nabla I(\vec{r},\widehat{\Omega},t) \right) \frac{ds}{c} \tag{2.42}$$

and $I(\vec{r} + c\widehat{\Omega}dt, \widehat{\Omega}, t + dt) = I(\vec{r},\widehat{\Omega},t)$, i.e. $dI = 0$ without any changes. However, the radiant energy has lost through absorption and scattering out of $\widehat{\Omega}$, radiant energy gained from scattering into $\widehat{\Omega}$, and from source emissions.

(ii) the amount of energy (per unit normal area per unit solid angle per unit time) absorbed in the small element of length ds is $\mu_a ds \times I(\vec{r},\widehat{\Omega},t)$.

(iii) the amount of energy scattered out of the direction $\widehat{\Omega}$, and into other angles $\widehat{\Omega}'$ that denotes as $\mu_s ds \times I(\vec{r},\widehat{\Omega},t)$.

(iv) and the amount of scattered light into the direction $\widehat{\Omega}$ from other angles $\widehat{\Omega}'$ are denoted as scattering integral over $\widehat{\Omega}'$, where the overall scattering probability is equivalent to $\mu_s ds$. As a scattering event occurs, the probability becomes $\sigma(\widehat{\Omega}',\widehat{\Omega})d\Omega'$ when the scattering occurs in the direction, $\widehat{\Omega}$ that comes from a solid angle, $d\Omega'$ around the other angle, $\widehat{\Omega}'$ (Hassan et al., 2015).

(v) the amount created by source terms is presented as $S(\vec{r},\widehat{\Omega},t)ds$.

Putting these together, the change in the radiance dI is determined by absorption from the beam, scattering out of the beam, scattering into the beam, and any emission into the beam from sources (Haskell et al., 1994). Thus, (2.43):

$$\begin{aligned} dI(\vec{r},\widehat{\Omega},t) &= -\mu_a(\vec{r}) I(\vec{r},\widehat{\Omega},t) ds - \mu_s(\vec{r}) I(\vec{r},\widehat{\Omega},t) ds \\ &+ \mu_s(\vec{r}) ds \int_{\widehat{\Omega}'} I(\vec{r},\widehat{\Omega}',t) \sigma(\widehat{\Omega}',\widehat{\Omega}) d\Omega' + S(\vec{r},\widehat{\Omega},t) ds \end{aligned} \tag{2.43}$$

Consequently, the radiance $I(\vec{r},\widehat{\Omega},t)$ satisfies the radiative transport equation (RTE) as,

$$\frac{1}{c}\frac{\partial I(\vec{r},\hat{\Omega},t)}{\partial t}+\hat{\Omega}.\nabla I(\vec{r},\hat{\Omega},t)+(\mu_a(\vec{r})+\mu_s(\vec{r}))I(\vec{r},\hat{\Omega},t)$$
$$=\mu_s(\vec{r})\int_{\hat{\Omega}'} I(\vec{r},\hat{\Omega}',t)\sigma(\hat{\Omega}',\hat{\Omega})d\Omega'+S(\vec{r},\hat{\Omega},t) \quad (2.44)$$

at position $\vec{r}$, and in an angular direction given by the unit vector, $\hat{\Omega}=(cos(\psi)\,sin(\theta),sin(\psi)\,sin(\theta),co\,s(\theta),c$ denotes the speed of light in the medium, $\mu_t(\vec{r})$ denotes the total interaction coefficient (absorption plus scattering), i.e. $\mu_t(\vec{r})=\mu_a(\vec{r})+\mu_s(\vec{r})$, and $\sigma(\hat{\Omega}',\hat{\Omega})$ is the normalised scattering cross-section (or phase function). The normalised scattering cross-section $\sigma(\hat{\Omega}',\hat{\Omega})d\hat{\Omega}'$ represents the probability of a photon incident at a scattering centre, from some direction $\hat{\Omega}$, that scattered into a solid angle $d\Omega'=\sin(\theta')\,d\theta' d\psi'$ around $\hat{\Omega}'$. Therefore, the first term on the right-hand side in (2.44), represents the sum of contributions of scattering events, from all directions $\hat{\Omega}'$, into the direction $\hat{\Omega}$ (Haskell et al., 1994). When scattering events are considered into angle $\hat{\Omega}$, it must have come from some direction $\hat{\Omega}'$ and the normalisation modify the integral of $\sigma(\hat{\Omega}',\hat{\Omega})d\hat{\Omega}'$ equal to 1, as in (2.45),

$$\int_{\hat{\Omega}'}\sigma(\hat{\Omega}',\hat{\Omega})d\Omega'=\int_0^{\pi}sin(\theta')d\theta'\int_0^{2\pi}\sigma(\theta',\psi',\hat{\Omega})d\psi'=1=\int_{\hat{\Omega}}\sigma(\hat{\Omega}',\hat{\Omega})d\hat{\Omega} \quad (2.45)$$

The final integral above holds as scattering from a fixed direction $\hat{\Omega}'$ that must be scattered into some angle $\hat{\Omega}$.

The second term on the right-hand side of (2.45) denotes a source term that the radiative energy in a solid angle $d\Omega$ in the direction $\hat{\Omega}$ which created in a time interval, dt in a volume dV around $\vec{r}$ is $S(\vec{r},\hat{\Omega},t)dVd\Omega dt$. The equation indicates that the scattering parameters $\mu_a(\vec{r})$ and $\mu_s(\vec{r})$ can be position-dependent which generally allows one to suppress the position dependence of $\sigma(\hat{\Omega}',\hat{\Omega})$ (Chandrasekhar., 1950). In this study, this means that the asymmetry parameter of g has become a function of position or more particularly as $g=g(z)$. Like the speed of light, c is very much larger than the speed of change due to biological signals or responses, the system is considered as always in a pseudo-steady state that it may neglect the time dependence. For the cases considered in this study, the radiance has an azimuthal symmetry $I(\vec{r},\hat{\Omega}')$ with independent of ψ', i.e. $I(\vec{r},\hat{\Omega})\equiv I(\vec{r},\theta)$. In such cases, the scattering integral in (2.46) is simplified as,

$$\int_{\hat{\Omega}'} I(\vec{r},\hat{\Omega}')\sigma(\hat{\Omega}',\hat{\Omega})d\Omega'=\int_0^{\pi}sin(\hat{\theta}')I(\vec{r},\hat{\theta}')d\theta'\int_0^{2\pi}\sigma(\hat{\Omega}',\hat{\Omega})\,d\psi'=$$
$$\int_0^{\pi}sin(\hat{\theta}')f_0(\theta,\theta',\psi)I(\vec{r},\hat{\theta}')d\theta' \quad (2.46)$$

In layered tissue where μ_a and μ_s are dependent on the layer depth, z with the azimuthal symmetry of any source term $S(\vec{r},\theta)$. This means that the $I(\vec{r},\theta)$ only depends on (z,θ) with an isotropic source, i.e. $S(z,\theta)$ with independent of θ, then $S(z,\theta)=S(z)$. In such layered tissue, the expression becomes (2.47),

$$cos(\theta)\frac{\partial}{\partial z}I(z,\mu)+\mu_t(z)I(z,\theta)=\frac{\mu_s(z)}{2}\int_0^{\pi}sin(\theta)f(\theta,\theta')I(z,\hat{\theta}')d\theta'+S(z,\theta) \quad (2.47)$$

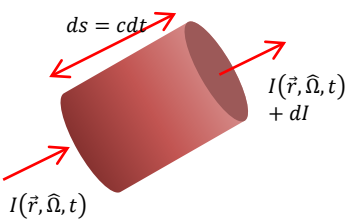

Figure 4: A graphical illustration of the diffusive cylinder

2.6 Diffusion Approximation – FEM Approach to obtain fluence rate

The average fluence rate, $\Phi(z)$ needs to be obtained for each tissue layer. To obtain the fluence rate, the radiance is integrated over its direction cosine (Tarvainen et al., 2006). Thus,

$$\boldsymbol{\Phi(z) = \int_0^{\pi} sin(\theta) I(z,\theta) d\theta} \tag{2.61}$$

and a flux vector $J(z)$ which describes the net flux of power (>0 in the z-direction, <0 in the direction of –z);

$$\boldsymbol{J(z) = \int_0^{\pi} \cos(\theta)\sin(\theta) I(z,\theta) d\theta} \tag{2.62}$$

The P_N-approximation corresponds to the radiance, I in terms of these angle-averaged, θ quantities as a sum of Legendre polynomial(s) in $cos\,(\theta)$, and the P_1-approximation that denotes as the lowest level approximation in the spectral radiation intensity, I (Reitzle et al., 2021).

$$I(z,\theta) \approx \Phi(z) + 3\cos(\theta) J(z) \tag{2.63}$$

Substituting (2.63) in the RTE equation, and using the normalization of (2.62) above, gives

$$\begin{aligned} &\cos(\theta)\frac{\partial}{\partial z}\Phi(z) + 3\cos^2(\theta)\frac{\partial}{\partial z}J(z) + \mu_t(z)\Phi(z) + 3\cos(\theta)J(z) \\ &\quad = \mu_s(z)\Phi(z) + 3\mu_s(z)J(z)\int_0^{\pi}\cos(\theta')\sin(\theta')\, f(\theta,\theta')d\theta' \\ &\quad + S(z) \end{aligned} \tag{2.64}$$

Multiplying (2.64) by $1/2\,sin(\theta)\,d\theta$ and integrating overall values of θ, the terms become proportional to $cos\,(\theta)$ will average to zero, while terms in $\cos^2(\theta)$ will average to 2/3. Next, multiplying (2.63) *by* $1/2cos\,(\theta)\,sin(\theta)\,d\theta$, integrating over θ and the terms in $\cos^3(\theta)$ is also vanish. Thus, the fluence rate becomes,

$$J(z) = -\frac{1}{3(\mu_a(z) + (1-g)\mu_s(z))}\frac{\partial}{\partial z}\Phi(z) = -D(z)\frac{\partial \Phi(z)}{\partial z} \tag{2.65}$$

Note that, the (2.65) becomes,

$$\Phi(z) = -\frac{1}{\mu_a(z)}\left(\frac{\partial J(z)}{\partial z} - S(z)\right) \tag{2.66}$$

Combining these two equations gives the well-known Diffusion approximation (Hassan et al., 2015)(Yudovsky & Durkin, 2011) as expressed in (2.67). However, this equation must be solved with appropriate boundary conditions.

$$\frac{\partial}{\partial z}\left(D(z)\frac{\partial \Phi(z)}{\partial z}\right) = \mu_a(z)\Phi(z) - S(z) \tag{2.67}$$

2.7 Boundary condition for P_1 Approximation

There are a variety of diverse ways of making the P_1 approximation meet the realistic boundary conditions (Reitzle et al., 2021). In this study, the simplest form of Marshak boundary condition at $z = 0$ is used to explain the flux density along with the tissue layers (Elshin et al., 2018)(Haskell et al., 1994). If the inward radiance, I at $z = 0$ is equivalent to $I_+(0,\theta)$, the Marshak scheme seeks to

match the actual total (integrated) of incoming energy that proportional to $cos\ (\theta)I_+(0,\theta)$ and to the total integrated P_1 of incoming flux accounted for $cos\ (\theta)I(0,\theta)$ where;

$$I(0,\theta) \approx\ \Phi(0) +\ 3\cos\ (\theta)J(0) \tag{2.71}$$

By integrating the equation by $\cos(\theta)\frac{1}{2}\sin(\theta)\mathrm{d}\theta)$ over $0 \le \theta \le \pi/2$ and it gives the true value of fluence rate in term of intensity, I ,

$$\frac{1}{4}\Phi(0) + \frac{1}{2}J(0) = \frac{1}{2}\int_0^{\pi/2} \cos\ (\theta)\sin(\theta)I_+(0,\theta)\mathrm{d}\theta \tag{2.72}$$

If there is no incoming radiance (i.e. $I_+(0,\theta) = 0$), the surface (z=0) current density, J becomes,

$$J(0) = -\frac{\Phi(0)}{2} \tag{2.73}$$

The fluence rate close to the surface is interpreted by Taylor's theorem in (2.73). Thus, there is an extrapolated point $z = z_B = -2D(0)$, at which the average fluence rate is zero.

$$\Phi(z) \approx\ \Phi(0) + z\frac{d\Phi(0)}{dz} = \Phi(0)\left(1 + \frac{\mathrm{z}}{2D(0)}\right) \tag{2.74}$$

In this study, a change in refractive index, R made the analysis more complex when the light flux, Φ leaves the medium. Therefore, a Fresnel reflectivity for normal incidence (Haskell et al., 1994) has been used in this study,

$$R = \frac{n-1}{n+1} \tag{2.75}$$

2.8 Transport Approximation to produce DC and AC component

In general, the Diffusion or P_1 approximation corresponds to strong and fairly isotropic scattering which is not particularly the case in the retina because there may be a large forward component and a somewhat weaker backscattered component (Hassan et al., 2015)**.** The Transport approximation gives details of light interaction in tissue that included the backscattered component which explained the amount of flux coming out of the surface. During retinal imaging photoplethysmography assessment, the Transport approximation assumed the scattering cross probability is given by a forward scattered peak, and the isotropic off-axis component (Dwyer & Matthew, 1985)(Hassan et al., 2015)**.** The Transport approximation phase function used for this work is expressed in (2.81),

$$\begin{aligned} &cos(\theta)\frac{\partial}{\partial z}I(z,\theta) + (\mu_a(z) + (1-g(z))\mu_s(z))I(z,\theta) \\ &\quad = \mu_s(z)\left(\frac{1-g(z)}{2}\right)\int_0^{\pi} sin(\theta)\, I\left(z,\hat{\theta}'\right)d\theta' \end{aligned} \tag{2.81}$$

and the un-scattered light in source term, $S(z)$

$$S(z) = \frac{S_0}{2}\mu_{tr}(z)\exp\left(-\int_0^z (\mu_a(z') + \mu_{tr}(z'))dz'\right) \tag{2.82}$$

The (2.81) and (2.82) allows the derivation of the DC component and AC component. These equations are solved using a finite element method (FEM) where the 1D tissue model of retina, RPE, choroid, and sclera is divided into N elemental layers by the $N+1$ points z_0 as the retina top

surface, z_1, z_2, …, z_N and the sclera bottom surface. The fluence rate $\varphi(z)$ is then approximated as a sum of $N+1$ shape functions (Hamdy et al., 2017),

$$\varphi(z) \cong \tilde{\varphi}(z) = \sum_{n=0}^{N} c_n \theta_n(z) \tag{2.83}$$

where the $\theta_n(z)$ are shape function and c_n represents their weight in the fluence rate, $\varphi(z)$. The FEM solution is useful to determine the best c_n values for the assumed shape functions, $\theta_n(z)$ and to obtain an approximate solution (Tarvainen et al., 2006). However, the $\tilde{\varphi}(z)$ cannot satisfy the total Diffusion approximation in (2.84) due to identically resulting in a residual error.

$$\begin{aligned} &\frac{dJ(z)}{dz} - S\mu_{tr}(z)R_a(z)R_{tr}(z) + (\mu_a(z) + \mu_{tr}(z))\varphi(z) \\ &\quad = 0 \qquad \text{and} \qquad J(z) = -D(z)\frac{d\varphi(z)}{dz} \end{aligned} \tag{2.84}$$

Thus, imposing the weak form requirement can ensure that the residual is orthogonal to all shape function and the error between $\varphi(z)$ and $\tilde{\varphi}(z)$ produced further by alternating the coefficient, $\underline{c}$. Imposing the orthogonal condition, the $\underline{c}$ must satisfy the (2.85),

$$\int_0^L \frac{d\tilde{J}(z)}{dz}\theta_m(z)dz + \int_0^L \mu_{tot}(z)\tilde{\varphi}(z)\theta_m(z)dz - S\int_0^L \mu_{tr}(z)R_a(z)R_{tr}(z)\theta_m(z)dz = 0 \tag{2.85}$$

To proceed further with the approximate solution, the shape function properties, $\theta_n(z)$ and the mesh points are specified. Here, the mesh is the set of points $m_0 := \{z_0 = 0, z_1, z_2, \dots, z_{N-1}, z_N = L\}$, and triangular Chapeaux shape functions are used (J. N. Reddy, 2019), as shown in **Figure 5**.

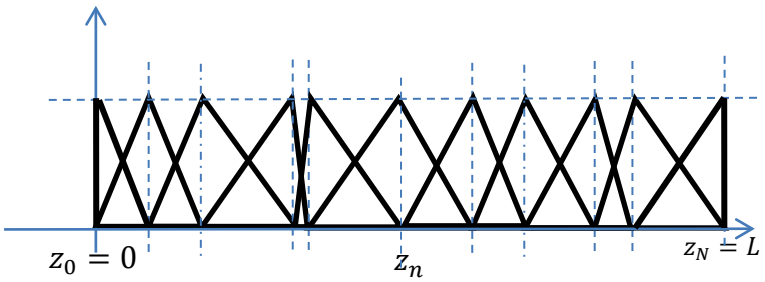

Figure 5: Chapeaux function at mesh points z_n

The Chapeaux shape functions, for $n \neq 0, N$, are defined as in (2.86);

$$\theta_n(z) = \begin{cases} \dfrac{z - z_{n-1}}{z_n - z_{n-1}} & \text{for } z_{n-1} < z < z_n \\ \dfrac{z_{n+1} - z}{z_{n+1} - z_n} & \text{for } z_n < z < z_{n+1} \end{cases} \tag{2.86}$$

and zero elsewhere. Then, with mass and stiffness matrices defined respectively,

$$\begin{aligned} M_{n,n+1} &= \int_0^L \mu_{tot}(z)\theta_n(x)\theta_{n+1}(z)dz = \mu_{tot,n}\int_{z_n}^{z_{n+1}} \theta_n(z)\theta_{n+1}(z)dz \\ K_{n,n+1} &= \int_0^L D(z)\frac{d\theta_n(z)}{dz}\frac{d\theta_{n+1}(z)}{dz}dz \end{aligned} \tag{2.87}$$

Combined the (2.86) and (2.87) the matrix equation become as (2.88):

$$SB_m = \sum_{n=0}^{N} (K_{m,n} + K_{m,n}^{+} + M_{m,n})c_n = [(K + K^{+} + M)c]_m \tag{2.88}$$

There are two common methods of representing the pulsatile (AC component) effects of a cardiac in a blood vessel embedded in the retina and choroid layer.

(i) The first method is to model the changing blood volume during the cardiac cycle by a time-dependent variation of the diameter of the vessel (Hassan et al., 2015)**.** Suppose that, a blood vessel, bv in the retinal layer in **Figure 2(b)** is located at the centre of depth, z_{bv} with diameter, $R_a(z)$ of absorption over the cycle that varies according to $d(t) = d_0 + \Delta(t)$, where d_0 the minimum value of its diameter with the definition of $\Delta(t) \geq 0$. This alters the function $R_a(z)$ over the cycle, through its dependence on the depth integral of $\mu_a(z)$. For $z < z_{bv} - d(t)$, the function of $R_a(z)$ is unchanged. For $z > z_{bv} + d(t)$, the two regions are considered (i) $z_{bv} - d(t) < z < z_{bv} - d_0$ and (ii) $z_{bv} + d_0 < z < z_{bv} + d(t)$ have their absorption changed from $\mu_{a,ret}$ (the retinal absorption) to $\mu_{a,bv} > \mu_{a,ret}$, the blood vessel absorption. Thus $\int_0^z \mu_a(z')dz'$ increases by $2(\mu_{a,bv} - \mu_{a,ret})\Delta(t)$. The same increase could be obtained by keeping the geometry the same that will not be increasing the blood vessel diameter and the absorption in the region $z_{bv} - d_0 < z < z_{bv} + d_0$ to $\mu_{a,bv}{}'(t) = \mu_{a,bv} + (\mu_{a,bv} - \mu_{a,ret})\Delta(t)/d_0$. By changing the scattering cross-section in the blood vessel can similarly mimic a change in diameter for the function $R_{tr}(z)$ transmittance in the *z-direction*.

(ii) This defines the second method, by keeping the same geometry and alter the absorption and scattering parameters with time. From the P_1 or Diffusion approximation equation for the fluence rate $\varphi(z)$ (Hassan et al., 2015) in (2.89),

$$\frac{d}{dz}\left(\frac{1}{3(\mu_a(z) + \mu_{tr}(z))}\frac{d\varphi(z)}{dz}\right) - \mu_a(z)\varphi(z) = S_1\mu_{tr}(z)R_a(z)R_{tr}(z) \tag{2.89}$$

These two methods will not give the same result even though the appropriate changes to the factors of absorption function, $R_a(z)$ and transmittance function, $R_{tr}(z)$ can be made in either way. The former would have unchanged optical parameters $\mu_a(z)$ and $\mu_{tr}(z)$, while the latter would have time-varying values. As these optical parameters appear differently in the first term, it gives a different equation for the two cases. Consequently, in the present work (Hassan et al., 2018)**,** the blood volume is varied to indicate the passage of a cardiac cycle. This was implemented by varying the geometry with time and fixed optical parameters.

3. Results

The interaction between light and matter such as morphology, dimension (area) of a scattering cross-section, and scattering properties of tissue components is crucial in diagnostic application to detect tissue structure abnormalities due to the diseases. In therapeutic applications, the changes of scattering properties in affected tissue provide significant information of optimal light delivery, reaction, and response during therapy. A 1D eye tissue model was developed to execute a fast computation process and a preliminary prediction of blood perfusion analysis using the Diffusion approximation - FEM approach. The blood perfusion analysis was demonstrated in oxy-haemoglobin 570 nm to obtain: (i) blood perfusion extraction in retina layer, (ii) blood perfusion in choroid layer, (iii) fluence rate in retina layer, and (iv) fluence rate in choroid layer.

3.1 Extraction of retinal blood perfusion and fluence rate

3.11 Case I: Blood perfusion in retina layer

The blood perfusion in the retina layer was obtained by quantifying the blood volume during the cardiac activity (systolic and diastolic). This blood volume was interpreted as the amplitude of a sinusoidal signal since the foundation of the PPG signal is a sinusoidal signal. The blood perfusion was extracted from the retina layer as shown in **Figure 6(a)**. The observation showed that the amplitude of the perfusion was approximately 0.0350 a.u (intensity) at 0.5s.

3.12 Case II: Blood perfusion in the choroid layer

The blood perfusion in the choroid layer was obtained by quantifying the blood volume in the blood vessel during cardiac activity. The time interval between the cardiac cycle is approximately 0.9 to 1.2 seconds. The blood perfusion in the vessel was interpreted as the amplitude of the sinusoidal signal. By observation in **Figure 6(b)**, the amplitude of the signal was approximately 0.0207 a.u (intensity) at 0.5s.

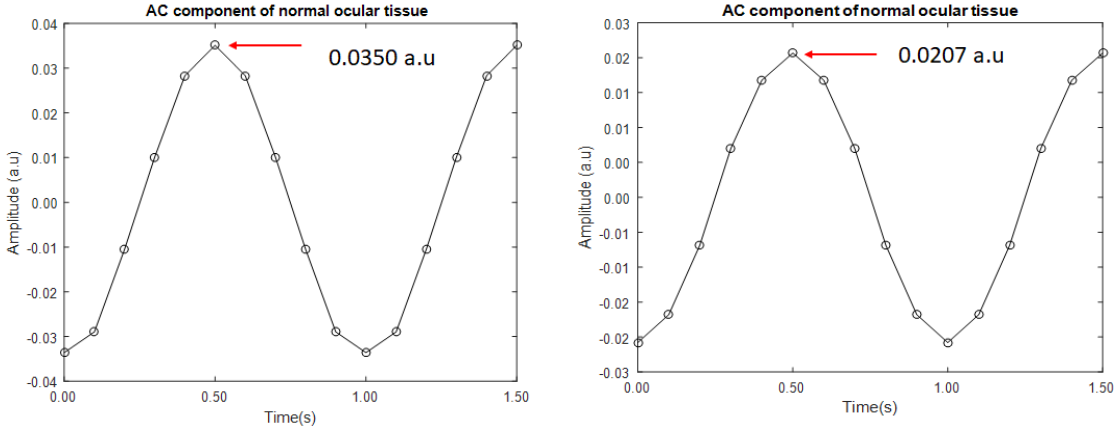

(a) (b)

Figure 6: (a) Blood perfusion in retina layer, (b) Blood perfusion in the choroid layer

3.13 Case I: Fluence rate in retina layer

In **Figure 7(a)**, the absorption coefficient, μ_a at a depth between 70 to 130 μm was higher than μ_s retina layer as tabulated in **Table 1**. A large number of photons were absorbed by melanin and blood in the retinal layer and the photon propagation stopped at depth of 1020 μm when the photons reach the bottom of the tissue. The flux density captured from the tissue surface, the retina layer to the sclera layer can be interpreted through a fluence rate mapping. The fluence rate started at (0,0.5) and decayed rapidly after the light passed the retina and the RPE layer at depth of 90 μm in **Figure 7(b)**. In the figure, the dashed line presents the boundary of each layer. The blood vessel layer in the depth between 80 μm to 120 μm can be seen along 200 μm of retina thickness. The extrapolated point, z in the figure demonstrated there was no incoming flux near the tissue surface before the retina layer.

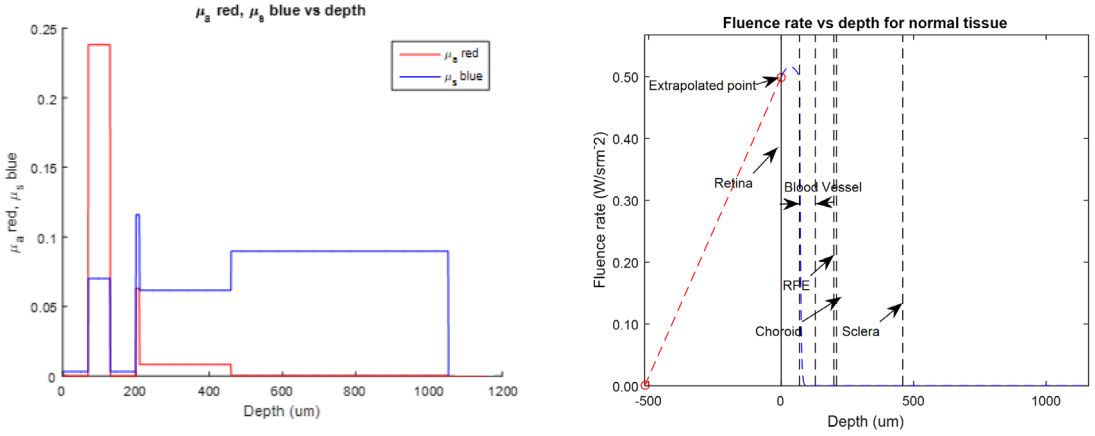

(a) (b)

Figure 7: Case I (a) Absorption and scattering coefficient versus the depth for healthy tissue in *oxy-haemoglobin* condition at 570 nm, (b) Fluence rate for healthy tissue versus the depth for healthy tissue in *oxy-haemoglobin* condition at 570 nm

3.14 Case II: Fluence rate in the choroid layer

Figure 8(a) presented the absorption, μ_a and the scattering coefficient, μ_s versus the depth for healthy tissue. In the figure, the scattering coefficient, μ_s has a higher coefficient than the coefficient absorption, μ_a at a depth between 200 to 210 μm when the photons traveled into the retina, RPE layer, and choroid layer. In **Figure 8(b)**, the fluent rate started at (0,1.00) and gradually decayed when the photon traveled across the choroid layer and the blood vessel at the depth of 200 to 294 μm.

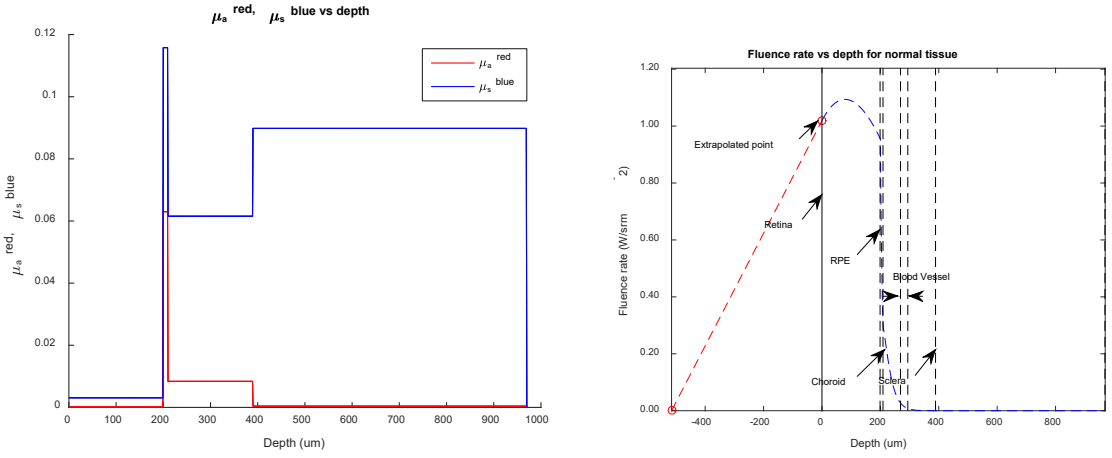

(a) (b)

Figure 8: Case II (a) Absorption and scattering coefficient versus the depth for healthy tissue in *oxy-haemoglobin* condition at 570 nm, (b) Fluence rate for healthy tissue versus the depth for healthy tissue in *oxy-haemoglobin* condition at 570 nm.

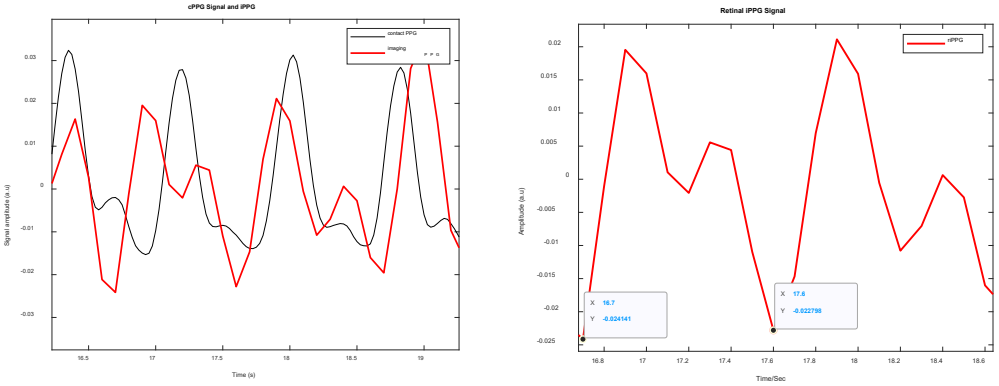

(a) (b)

Figure 9: (a) Mapping contact PPG signal due to cardiac activity and retinal imaging PPG signal from experimental work (b) A sample of retinal iPPG signal from a subject eye.

Figure 9(a) presented a mapping of contact PPG due to cardiac activity using a pulse oximeter and retinal imaging PPG signal was extracted from a subject fundus video during experimental work. **Figure 9(b)** showed the trough differences of retinal PPG signal was approximately 0.9 which is within the range of heartbeat 0.9 to 1.5 seconds.

4. Discussion

The blood carries nutrients, enzymes, and oxygen that are useful for the eye tissue. The information of blood perfusion in the eye is essential to identify blood flow abnormality in the blood vessel that is related to diseases such as diabetes, glaucoma, hypertension, ischemia heart, etc (Flammer et al., 2013)**.** A normal blood velocity in veins is two times the velocity in the arteries. The veins diameter is much bigger than the arteries that allow a sufficient amount of blood from the heart to back to the arteries (Golzan et al., 2012). In Case I, the absorption coefficient, μ_a was set up higher than the scattering coefficient, μ_s as tabulated in **Table 1**. A large number of photons were absorbed by the melanin in the retina, RPE, and blood which has left some photons to propagate deeper into the tissue, and quite a large number of scattered photons were emitted back to the tissue surface as backscattering light. These backscattering lights were captured by the camera during retinal imaging PPG assessment and translated as an imaging PPG signal and it was interpreted as a sinusoidal signal in **Figure 6(a)**. In **Figure 6(b)** of Case II, the scattering coefficient, μ_s was set up higher than the absorption coefficient, μ_a. This increased the chances of a large number of photons to traveled deeper to the choroid layer and emitted to the tissue surface. However, there were quite many photons being absorbed by the blood for the second time before reaching the tissue surface. Therefore, the visibility of blood perfusion to be seen from the choroid layer was quite challenging using retinal imaging PPG compared to the retina layer, since it was located closer to the tissue surface.

The light fluence distribution is important to ensure a successful photodynamic therapy treatment (PDT). Therefore, it is important to assess the rate of photochemical reaction on the treated tissue as it depends on the light dose delivered on the tissue. The light rate distribution can be influenced by optical properties, tissue geometry, and irradiation geometry (Steven L Jacques & Pogue, 2008)(Haskell et al., 1994)**.** The diffusion theory offered simplicity that quantifies fluence rate accurately in scattering media such as eye tissue. **Figure 7(a)**, showed the fluence rate of the flux surface that satisfied the absorption coefficient, μ_a and scattering coefficient, μ_s set up along with the depth of the healthy tissue. The optical properties setting in **Table 1** was set up with an absorption coefficient, μ_a higher than the scattering coefficient, μ_s. The photons propagated into the tissue as soon as the light beam hit the tissue surface went into the retina, RPE, and the closest blood vessel. In **Figure 7(b)** of Case I, the flux rate was high as soon as the photons started to

travel into the retina at depth 200 μm. However, the flux rate was decayed rapidly at (0,0.50) when the photons reached RPE and blood vessels where most of the absorption and scattering events happened between the retina, RPE, and blood vessels. In the figure, the extrapolated point $z = z_B = -2D(0)$, where the average fluence rate at the surface was zero before the photon reached the retina. In **Figure 8(a)** of Case II, the scattering coefficient, μ_s was set up higher than the absorption coefficient, μ_a which has increased the chances of photons reached the bottom layer of the tissue. The absorption event mostly happened in the retina and RPE due to the presence of blood. However, in **Figure 8(b)**, the extrapolated point z in Case II started to slowly decay at (0, 1.00) after 200 μm after the photon reached the choroid layer and blood vessel. This indicates that most of the photons were absorbed by the blood compared to melanin in the RPE layer. In **Figure 9(a)** and **9(b)**, the contract PPG signal was mapped with retinal imaging PPG signal. The trough difference of the retinal imaging PPG signal was 0.9 seconds which in the range of 0.9 to 1.5 seconds of the heartbeat. These results showed that the retinal imaging PPG signal has a combination of sinusoidal (sin ωt) and cosine (cos ωt) waveform that relates to systolic and diastolic blood pressure due to cardiac activity.

5. Conclusion

The 1D diffusion approximation-FEM approach was modeled in the *z-direction* to quantify the amplitude of AC signal as a response produced during blood flowing in the blood vessel. The simulations of the 1D diffusion approximation model are performed on healthy tissue in the retina and choroid layer. Also, the investigation has extended to observe the fluent rate in both layers that are influenced by the scattering and absorption coefficient.

The observation of AC has concluded that the amplitude of AC components was not significantly affected by the variation of blood vessel diameter, but the amplitude changes are most likely affected by the blood vessel position and the decrease of scattering coefficient, μ_s. In Case I the extrapolated point $z = z_B = -2D(0)$, decay rapidly as soon as the photon hits the retina where the absorption coefficient was high when there was the presence of melanin and blood. In Case II, the scattering coefficient, μ_s was high where the chances of photons reaching the bottom layer were also high. However, the photons were absorbed two times to reach the surface that soon interpreted as backscattering light. The light distribution described by diffusion theory was less accurate when demonstrated on the eye tissue where the tissue layers were thin and close to sources and boundaries (Jia et al., 2021) Also, the validity of photon distribution theory satisfied $\mu_s << \mu_s'$ for most biological tissue at visible to near-infrared wavelength**.** However, the developed 1D diffusion approximation-FEM approach model was capable to demonstrate a fast computation process and can be used as a preliminary prediction of blood perfusion analysis without concerning the stochastic noise produced during the calculations. The investigation of light quantification and interaction will be extended using 3D Monte Carlo technique for future work.

Acknowledgment

This work was financially supported by Universiti Teknologi MARA, Shah Alam, Malaysia under RMI Geran Penyelidikan Khas 600-RMC/GPK/5/3(156/2020).

References

Atchison, D. A., Markwell, E. L., Kasthurirangan, S., Pope, J. M., Smith, G., & Swann, P. G. (2008). Age-related changes in optical and biometric characteristics of emmetropic eyes. *Journal of Vision*, *8*(4), 29. https://doi.org/10.1167/8.4.29

Beyer, T., Bidaut, L., Dickson, J., Kachelriess, M., Kiessling, F., Leitgeb, R., Ma, J., Shiyam Sundar, L. K., Theek, B., & Mawlawi, O. (2020). What scans we will read: imaging instrumentation trends in clinical oncology. *Cancer Imaging*, *20*(1), 38. https://doi.org/10.1186/s40644-020-00312-3

Chandrasekhar., S. (1950). Radiative transfer. London (Oxford University Press). *Quarterly Journal of the Royal Meteorological Society*, *76*(330), 498. https://doi.org/https://doi.org/10.1002/qj.49707633016

D.J., B. (2012). Pathophysiology of Retinal Vein Occlusions. In: Retinal Vein Occlusions. In *Retinal Vein Occlusions* (1st ed., pp. 33–72). Springer International Publishing. https://doi.org/10.1007/978-1-4614-3439-9_2

Dwyer, V. M., & Matthew, J. A. D. (1985). A comparison of electron transport in AES/PES with neutron transport theory. *Surface Science*, *152–153*, 884–894. https://doi.org/https://doi.org/10.1016/0039-6028(85)90501-1

Eliasdottir, T. S. (2018). Retinal oximetry and systemic arterial oxygen levels. *Acta Ophthalmologica*, *96*(A113), 1–44. https://doi.org/https://doi.org/10.1111/aos.13932

Elshin, A. V., Muraveva, K. V., Borisenko, A. I., & Kalutik, A. A. (2018). Mark and Marshak boundary conditions in surface harmonics method. *Journal of Physics: Conference Series*, *1133*(1). https://doi.org/10.1088/1742-6596/1133/1/012017

Fass, L. (2008). Imaging and cancer: a review. *Molecular Oncology*, *2*(2), 115–152. https://doi.org/10.1016/j.molonc.2008.04.001

Flammer, J., Konieczka, K., Bruno, R. M., Virdis, A., Flammer, A. J., & Taddei, S. (2013). The eye and the heart. *European Heart Journal*, *34*(17), 1270–1278. https://doi.org/10.1093/eurheartj/eht023

Golzan, S. M., Avolio, A., & Graham, S. L. (2012). Hemodynamic Interactions in the Eye: A Review. *Ophthalmologica*, *228*(4), 214–221. https://doi.org/10.1159/000342157

Hamdy, O., El-Azab, J., Al-Saeed, T. A., Hassan, M. F., & Solouma, N. H. (2017). A Method for Medical Diagnosis Based on Optical Fluence Rate Distribution at Tissue Surface. *Materials (Basel, Switzerland)*, *10*(9). https://doi.org/10.3390/ma10091104

Handapangoda, C. C. (2017). Modeling and numerical simulation of light propagation through biological tissue with implanted structures. *Thesis*, *Monash University. Thesis.*, https://doi.org/10.4225/03/587c04bcdc2eb.

Hani, A., Nugroho, H. A., Nugroho, H., & Izhar, L. I. (2009). Contrast Enhancement of Retinal Vasculature in Digital Fundus Image. *2009 International Conference on Digital Image Processing*, 137–141.

Haskell, R. C., Svaasand, L. O., Tsay, T.-T., Feng, T.-C., McAdams, M. S., & Tromberg, B. J. (1994). Boundary conditions for the diffusion equation in radiative transfer. *J. Opt. Soc. Am. A*, *11*(10), 2727–2741. https://doi.org/10.1364/JOSAA.11.002727

Hassan, H., Hu, S., & Dwyer, V. M. (2015). A dynamic opto-physiological model to effectively interpret retinal microvascular circulation. *Progress in Biomedical Optics and Imaging - Proceedings of SPIE*, *9315*. https://doi.org/10.1117/12.2076899

Hassan, H., Jaidka, S., Dwyer, V. M., & Hu, S. (2018). Assessing blood vessel perfusion and vital signs through retinal imaging photoplethysmography. *Biomedical Optics Express*, *9*(5). https://doi.org/10.1364/BOE.9.002351

Henyey, L. ~G., & Greenstein, J. ~L. (1941). Diffuse radiation in the Galaxy. *apj*, *93*, 70–83. https://doi.org/10.1086/144246

J. N. Reddy, P. D. (2019). *Introduction to the Finite Element Method, Fourth Edition* (4th editio). McGraw-Hill Education. https://www.accessengineeringlibrary.com/content/book/9781259861901

Jacques, S L. (1998). Path integral description of light transport in tissue. *Annals of the New York Academy of Sciences*, *838*, 1–13. https://doi.org/10.1111/j.1749-6632.1998.tb08183.x

Jacques, Steven L. (2013). Optical properties of biological tissues: a review. *Physics in Medicine and Biology*, *58*(11), R37–R61. https://doi.org/10.1088/0031-9155/58/11/r37

Jacques, Steven L, & Pogue, B. W. (2008). Tutorial on diffuse light transport. *Journal of Biomedical Optics*, *13*(4), 1–19. https://doi.org/10.1117/1.2967535

Jia, H., Chen, B., & Li, D. (2021). Accurate Simulation of Light Propagation in Complex Skin Tissues Using an Improved Tetrahedron-Based Monte Carlo Method. *Applied Sciences*, *11*(7). https://doi.org/10.3390/app11072998

Kim, A. D., & Keller, J. B. (2003). Light propagation in biological tissue. *J. Opt. Soc. Am. A*, *20*(1), 92–98. https://doi.org/10.1364/JOSAA.20.000092

Liu, W., Jiao, S., & Zhang, H. F. (2013). Accuracy of retinal oximetry: a Monte Carlo investigation. *Journal of Biomedical Optics*, *18*(6), 66003.

https://doi.org/10.1117/1.JBO.18.6.066003
Morgan, W. H., Abdul-Rahman, A., Yu, D.-Y., Hazelton, M. L., Betz-Stablein, B., & Lind, C. R. P. (2015). Objective Detection of Retinal Vessel Pulsation. *PLOS ONE*, *10*(2), e0116475. https://doi.org/10.1371/journal.pone.0116475
Morgan, W. H., Hazelton, M. L., Betz-Stablein, B. D., Yu, D.-Y., Lind, C. R. P., Ravichandran, V., & House, P. H. (2014). Photoplethysmographic Measurement of Various Retinal Vascular Pulsation Parameters and Measurement of the Venous Phase Delay. *Investigative Ophthalmology & Visual Science*, *55*(9), 5998–6006. https://doi.org/10.1167/iovs.14-15104
Reitzle, D., Geiger, S., Liemert, A., & Kienle, A. (2021). Semianalytical solution for the transient temperature in a scattering and absorbing slab consisting of three layers heated by a light source. *Scientific Reports*, *11*(1), 8424. https://doi.org/10.1038/s41598-021-87030-3
Rodmell, P. I., Crowe, J. A., Gorman, A., Harvey, A. R., Muyo, G., Mordant, D. J., M.D., A. I. M., & Morgan, S. P. (2014). Light path-length distributions within the retina. *Journal of Biomedical Optics*, *19*(3), 1–9. https://doi.org/10.1117/1.JBO.19.3.036008
Simon, E., Foschum, F., & Kienle, A. (2013). Hybrid Green's function of the time-dependent radiative transfer equation for anisotropically scattering semi-infinite media. *Journal of Biomedical Optics*, *18*(1), 1–7. https://doi.org/10.1117/1.JBO.18.1.015001
Tarvainen, T., Vauhkonen, M., Kolehmainen, V., & Kaipio, J. P. (2006). Finite element model for the coupled radiative transfer equation and diffusion approximation. *International Journal for Numerical Methods in Engineering*, *65*(3), 383–405. https://doi.org/https://doi.org/10.1002/nme.1451
Tornow, R.-P., Kolar, R., Odstrcilik, J., Labounkova, I., & Horn, F. (2021). Imaging video plethysmography shows reduced signal amplitude in glaucoma patients in the area of the microvascular tissue of the optic nerve head. *Graefe's Archive for Clinical and Experimental Ophthalmology*, *259*(2), 483–494. https://doi.org/10.1007/s00417-020-04934-y
Yudovsky, D., & Durkin, A. J. (2011). Hybrid diffusion and two-flux approximation for multilayered tissue light propagation modeling. *Applied Optics*, *50*(21), 4237–4245. https://doi.org/10.1364/AO.50.004237

2021 ICMS

INTERNATIONAL CONFERENCE ON COMPUTING, MATHEMATICS AND STATISTICS

e ISBN 978-967-2948-12-4

9 7 8 9 6 7 2 9 4 8 1 2 4